

1        **Micro- and nano-scale study of deformation induced mineral**  
2        **transformations in Mg-phyllosilicate-rich fault gouges from the**  
3        **Galera Fault Zone (Betic Cordillera, SE Spain)**

4        CATALINA SÁNCHEZ-ROA (1) \*, BLANCA BAULUZ (2), FERNANDO NIETO (3), ISABEL ABAD (1), JUAN  
5        JIMENÉZ-MILLÁN (1) DANIEL FAULKNER (4).

6        (1) Departamento de Geología and CEACTierra, Unidad Asociada IACT (CSIC-UGR), Universidad de  
7        Jaén, Campus Las Lagunillas s/n, 23071 Jaén, Spain, (2), IUCA-Facultad de Ciencias, Universidad de  
8        Zaragoza, Pedro Cerbuna 12, Zaragoza, Spain, (3) Departamento de Mineralogía y Petrología and IACT  
9        (CSIC-UGR), Facultad de Ciencias, Universidad de Granada, Avda. Fuentenueva s/n, 18002 Granada,  
10        Spain, (4) Rock Deformation Laboratory, Department of Earth, Ocean and Ecological Sciences,  
11        University of Liverpool, Liverpool, UK.

12  
13        **Abstract**

14        Naturally and experimentally deformed gouges from sliding surfaces within the Galera Fault Zone  
15        were analyzed using scanning and transmission electron microscopy (SEM, TEM) to identify  
16        changes in the fault rocks as a consequence of ongoing deformation. The two gouges studied have  
17        a particular mineral association that includes planar (mainly smectite and illite) and fibrous clay  
18        minerals (sepiolite and palygorskite). Microstructural findings include a radical difference in grain  
19        alignment between the two gouges, a phenomenon that strongly influences gouge permeability.  
20        Smectite crystals are aligned on the same orientation and show a great number of layer terminations  
21        and delamination on the basal planes that contribute to a distributed mode of deformation in the  
22        gouge. In contrast, the sepiolite-rich gouge exhibits a grid-like microfabric that results in localized  
23        deformation limited to small areas where the needle-like crystals are bent and broken producing  
24        “feather-like” structures, without the presence of lattice distortions. Meanwhile, significant

25 chemical results include: 1. Al content identified in sepiolite fibers through Analytical Electron  
26 Microscopy (AEM), together with variability in the (110) d-spacing of sepiolite across single fibers,  
27 suggest the existence of a progressive transformation from sepiolite to palygorskite; 2. Mg content  
28 in smectite suggests that a portion of the smectites within the fault plane could have an authigenic  
29 origin and may be the result of a transformation reaction from palygorskite, however the similarity  
30 of the 2:1 layer compositions between the smectites in the two contexts do not allow to either  
31 confirm nor deny such possibility. 3. Chemical continuity of Mg-decrease and Al+Fe-increase in  
32 the octahedral cation content of the sepiolites, palygorskites and smectites within the gouges  
33 indicate a sequence of mineral transformations that is favored by a depleted Mg content and an  
34 increase of Al content in the fluid. In this setting, deformation promotes grain size reduction and  
35 fluid-rock interaction with the wall rocks resulting in a local supply of Al to the fault gouge that  
36 drives phase transformations. Structural differences between smectites and fibrous clay minerals  
37 affect important chemical and physical properties of the gouge including their mechanical  
38 properties. We propose that the permeability of the gouges in the Galera Fault is strongly affected  
39 by their mineralogy. Furthermore, the extent of the mineral authigenesis and mineral  
40 transformations could be a controlling factor that progressively change both the permeability and  
41 the strength of the fault.

42

43

**44 Keywords:**

45 Fibrous clay minerals, mineral transformations, fault zones, mineralogy of fault rocks, sepiolite,  
46 palygorskite, smectite, HR-TEM.

47

48

49

**50 1. Introduction**

51 Active faulting is an important phenomenon triggering chemical and physical processes in the  
52 rocks involved (Hickman et al., 1995; Faulkner et al., 2010). Chemical processes involve element  
53 mobility and redistribution assisted by fluids flowing through the faults. These fluids can either  
54 come from deep sources as in the case of hot springs, basin brines, hydrothermal and metamorphic  
55 fluids, or meteoric waters infiltrating through the newly-formed cracks in the rock. Significant  
56 evidence of the chemical reactions that occur in this setting include changes in the mineralogy of  
57 the fault gouge and adjacent rock (e.g., Sibson et al., 1979; Cox et al., 2001; Schleicher et al., 2006;  
58 2012). Physical processes on the other hand are related to how minerals accommodate  
59 deformation under high levels of strain, commonly experienced on fault planes. A previous study  
60 of the mineralogy of the Galera Fault (SE Spain) documented the presence of authigenic Mg-rich  
61 fibrous clay minerals within the fault planes as a consequence of the fluid-rock interactions favored  
62 by active faulting (Sánchez-Roa et al., 2016). The two types of fault gouge in the Galera Fault  
63 present different resistance to shear due to the authigenic minerals concentrated in each section  
64 of the fault: the gouge to the south-west, which is rich in fibrous clay minerals has a higher friction  
65 coefficient ( $\mu=0.47$  under wet deformation); meanwhile the gouge recovered close to the town of  
66 Galera is rich in smectite with a small amount of fibrous minerals and has a lower friction  
67 coefficient ( $\mu=0.17$  under wet deformation) (Sánchez-Roa et al., 2016). The contrasting  
68 mechanical behavior between the two gouges motivates the study of the textural evolution and  
69 mineral transformations that can contribute to a differential resistance to shear during active  
70 faulting.

71 Permeability is an important parameter in fault zones and is impacted by fundamental parameters  
72 such as the host rock lithology, fault activity, magnitude of displacement, pre-existing structures,  
73 the depth, the tectonic stress field and the width of the deformed zone (Houwens et al., 2015). The  
74 rock texture and its influence in the permeability of the two gouge types of the Galera Fault Zone

75 can be explored through scanning and transmission electron microscopy (SEM and TEM). A  
76 micro- and nano-scale study of these fault rocks could provide a deeper insight into the  
77 deformation mechanisms in phyllosilicates. Planar phyllosilicates commonly deform through  
78 delamination, fracturing, kinking and dislocation glide (Ibanez and Kronenberg, 1993; Mares and  
79 Kronenberg, 1993; Sánchez-Navas and Galindo-Zaldívar, 1993; French et al., 2015). Delamination  
80 often occurs during frictional sliding in phyllosilicates with low interlayer electrostatic separation  
81 energy (Moore and Lockner, 2004), as is the case for talc and pyrophyllite (Giese, 1978; Sakuma  
82 and Suehara, 2015). However, little is known about the possible deformation mechanisms and  
83 fluid/mineral interactions occurring in fibrous materials such as the fibrous clay minerals or a  
84 mixed regime where both fibrous and planar phyllosilicates are present.

85 TEM study of clay minerals is challenging due to their susceptibility to electron beam damage,  
86 which is mainly related to the diffusion of alkali elements induced by the high voltages of the  
87 electron beam (van der Pluijm et al., 1988; Peacor, 1992). These observations remain true for the  
88 fibrous clay mineral group (sepiolite and palygorskite), where the cause of instability under the  
89 electron beam has been previously attributed to the high percentage of H<sub>2</sub>O and mobile cations  
90 within the zeolite-like channels (Krekeler and Guggenheim, 2008). Most work on the microscopic  
91 properties of these minerals has been achieved by separating individual particles, however the  
92 investigation of their mineral transformations and their contribution to the fabric of rocks is still  
93 to be explored. Thus, the study of these minerals and their texture in the context of active  
94 deformation is poorly understood and requires TEM exploration.

95 In this study, we investigate naturally and experimentally deformed fault gouge samples from two  
96 main shear zones within the Galera Fault Zone by SEM and TEM. The aim of the study is to  
97 identify the microstructural features and mineral transformations that contribute to differences in  
98 the resistance to shear between the two main shear zones of the Galera Fault Zone.

99

## 100 2. Geological setting and materials

101 The Galera Fault Zone is an active strike-slip fault (Fig. 1), located in the Betic Cordillera of  
102 southeast Spain within the Guadix-Baza Basin (García-Tortosa et al., 2011). The Galera Fault has  
103 an extension of approximately 23 km long and 1.5 km wide with orientation N50°E. The structure  
104 is associated with a NE–SW elongated asymmetric anticline and consists of several parallel splays  
105 dipping 40° to 60° NW (Sánchez-Roa et al., 2016). The sedimentary sequence of the wall rock  
106 presents an alternation of white marls and dark lutitic layers that contain dolomite, gypsum, quartz,  
107 calcite and phyllosilicates in their mineral assemblages. Two distinct minerals assemblages have  
108 been identified within the fault planes and are focus of this study. The first consists of smectite-  
109 and palygorskite-rich fault gouges at the central area of the fault (Galera Village); the second  
110 consists of a sepiolite-rich gouge mainly at the SW segment of the fault (Rambla de los Pilares).  
111 Fibrous clay-rich gouges are enriched in Mg due to hydrothermal alteration during periods of fluid-  
112 rock interaction, concentrated in fault planes and fractures (Sánchez-Roa et al., 2016).

113

114

115

### 116 3. Methods

#### 117 3.1. Sample preparation

118 The preparation of samples for High-Resolution (HR-) TEM observation had three different  
119 procedures:

##### 120 3.1.1 Impregnation with London Resin White (LRW) and ion thinning

121 Samples selected for microstructural analysis were prepared using a method modified from Kim  
122 et al. (1995). The method involves a multi-step exchange of the sample material with ethanol  
123 (99.9%) and London Resin White under refrigeration. The aim of the impregnation is to preserve  
124 the texture and the permanent expansion of smectite interlayers for TEM observation.

125 The impregnation of samples involves a hydration phase, where air-dried rock pieces were placed  
126 on a grid suspended over water creating a water steam saturated atmosphere. The samples were  
127 left for rehydration over a period of 48 hours. During the embedding phase: The water in the clay  
128 is replaced by ultra-pure ethanol of 99.9% purity. The samples were immersed in 100% ethanol  
129 for two periods of two hours and one of four hours. The LRW is progressively added in different  
130 mixtures of ethanol and LRW with volume ratios of  $\frac{1}{2}$ ,  $\frac{1}{3}$  and  $\frac{1}{4}$  each for two hours and then  
131 immersed in pure LRW overnight in a refrigerator. The next day the LRW was changed twice after  
132 periods of four hours. Finally, in the polymerization phase, fresh LRW was added to the samples  
133 and placed in an oven at 60 °C for 24h to polymerize and harden the LRW. The vacuum desiccator  
134 step (Kim et al., 1995), was not fully carried out due to the fragile nature of the samples.

135 The cured samples were cut perpendicular to the shear plane, in the direction of shear and an  
136 ordinary thin section was then prepared using a diamond saw with oil as lubricant to shape the  
137 samples. Sticky wax was used as an adhesive to bond the sample and the thin section glass.

138 Several 3 mm copper rings with a 1 mm hole in diameter were glued with an epoxy resin to the  
139 areas selected for further study. After drying for 24 hours, the rings were removed by heating the  
140 thin section. The rings were cleaned and ion-thinned to a suitable thickness for TEM study in a  
141 Fischione-1010 ion mill (Universidad de Jaén). The initial conditions for the ion thinning were 12°,  
142 5kV and 5mA until the first hole opened, from there they had an intermediate stage with 8°, 4kV  
143 and 5mA, followed by a final stage with 5°, 3kV and 5mA.

### 144 **3.1.2 Impregnation with Epothin resin and FIB-SEM**

145 Sample preparation through the second method included an impregnation of the samples in  
146 EpoThin resin and hardener in a ratio of 2:1 and hardened under vacuum. The blocks were  
147 polished using silicon carbide powder and both isopropanol and mineral oil as lubricant agent.  
148 The polished blocks were observed under a Dual Beam Ariga Zeiss FIB-SEM (Focused Ion Beam-  
149 Scanning Electron Microscope) mainly operated at 30kV (Universidad de Sevilla). The objective  
150 of using the technique is to identify the most interesting areas for observation while keeping the  
151 fabric and structural context of the extracted lamellae. The FIB-SEM technique combines imaging  
152 capabilities of the electron beam and milling capabilities of the ion beam allowing the selection of  
153 suitable sampling sites with signs of higher deformation and micro-scale sectioning of electron  
154 transparent foils for TEM analysis. The selected area is marked and trenched using a focused beam  
155 of Ga<sup>+</sup> ions (Overwijk, 1993), the initial intensity for trenching was set to 20 nA for one hour and  
156 then set to 4 nA until the end of the trenching process. The procedure leaves a narrow slice  
157 standing and pending by one of the uncut edges. The slice was then welded by depositing a Pt-  
158 binding agent and was fixed to a half-copper-washer for TEM observation.

### 159 **3.1.3 Particle dispersion**

160 Powders of the natural samples were prepared using holey carbon-coated Cu grids. The powder  
161 was dispersed in ultra-pure ethanol and immersed in the ultrasonic bath for 15 seconds. This  
162 preparation disperses individual grains of minerals onto the grid surface. The analyses performed

163 on individual crystals allow a larger area to be used in the scanning transmission electron  
164 microscopy (STEM) mode for the chemical quantitative analysis and provides better  
165 reproducibility of data due to the decrease in alkali loss. Although the powdered samples offer  
166 higher spatial resolution for chemical analysis using EDS, the ion-milled samples offer textural  
167 information of the analyzed grains (Abad et al., 2002).

168 In addition to the natural samples, homoionized specimens of the smectite-rich sample were also  
169 analyzed using this particle dispersion method to reveal the possible presence of interlayer Mg.

170

### 171 **3.2. Analytical techniques**

#### 172 **Scanning Electron Microscopy (SEM)**

173 Textural observations were made on polished impregnated blocks in secondary electron mode  
174 (SE) and backscattered electron mode (BSE). The SEM study was carried out with a Merlin Carl  
175 Zeiss field emission (FE) SEM in the Centro de Instrumentación Científico-Técnica of the  
176 Universidad de Jaén.

#### 177 **High-Resolution Transmission Electron Microscopy (HR-TEM)**

178 The TEM images were obtained using three instruments: a JEOL-2000-FX-II TEM at the  
179 University of Zaragoza operated at 200 kV; a FEI TITAN G2 TEM in the Centro de  
180 Instrumentación Científica (C.I.C.) of the Universidad de Granada, operated at 300 kV, with  
181 XFEG emission gun, spherical aberration corrector and HAADF detector, with a resolution of  
182 0.8 Å in the TEM mode and 2 Å in the scanning TEM mode; and a FEI TITAN High-Base TEM  
183 in the Laboratorio de Microscopias Avanzadas at the Universidad de Zaragoza, operated at 300  
184 kV, with Schottky-FEG emission gun, spherical aberration corrector (CETCOR, CEOS  
185 company), HAADF detector, and a 2k x 2k CCD Gatan camera, with a resolution of 0.9 Å in the  
186 TEM mode.



187 **Analytical Electron Microscopy (AEM)**

188 Chemical analyses (TEM-AEM) were obtained with two instruments: a Philips CM20 (C.I.C.,  
189 Universidad de Granada), operating at 200 kV in STEM mode, with an EDAX solid-state energy  
190 dispersive X-ray (EDX) detector and with a scan window of  $\sim 20 \text{ \AA} \sim 100 \text{ nm}$  for the analysis of  
191 individual clay particles; the second instrument is a FEI TITAN Low-base TEM in the Laboratorio  
192 de Microscopias Avanzadas at the Universidad de Zaragoza, operated at 300 kV, with a high  
193 brightness field emission gun (XFEG), a monochromator unit, a spherical aberration corrector  
194 (CETCOR, CEOS company), HAADF detector, and a 2k x 2k CCD Gatan camera, with a  
195 resolution of  $0.9 \text{ \AA}$ . The analyses were obtained in the HRSTEM mode. The following minerals  
196 were used to obtain the k factors for the transformation of intensity radiuses towards  
197 concentration ratios in accordance with the approximation made by Cliff and Lorimer (1975):  
198 albite, olivine, biotite, spessartine, muscovite, chlorite and titanite.

199 Structural formulas of smectites were calculated from AEM data after analyzing 103 crystals. The  
200 results were normalized to  $\text{O}_{10}(\text{OH})_2$  and all Fe was considered as  $\text{Fe}^{3+}$ . The normalization  
201 procedure shows a sum of octahedral cations higher than 2.1 per formula unit (a.f.u.) for 43% of  
202 the analyzed crystals indicating a divergence from their dioctahedral character. In addition, the  
203 sum of interlayer cations is lower than 0.2 a.f.u. for 32.5% and lower than 0.3 for 53.9% of the  
204 analyzed crystals. These results suggest the possibility that some of the  $\text{Mg}^{2+}$  that was originally  
205 considered octahedral is instead located in the interlayer. Analyses on smectite particles from the  
206 samples homoionized with K and Ca show a strong decrease in Mg content, an octahedral  
207 population very close to 2 a.f.u., and normal values of interlayer population. Based on these results,  
208 the total  $\text{Mg}^{2+}$  of the natural samples was redistributed within interlayer and octahedral positions  
209 to ensure that the octahedral sheet keeps a dioctahedral character and that the interlayer charge  
210 remains within the normal range for smectites (0.2 to 0.6).

### 211 3.3. Permeability measurements

212 Permeability tests were carried out on a triaxial deformation apparatus with a servo-controlled axial  
213 loading system and fluid pressure pump (Mitchell and Faulkner, 2008) in the Rock Deformation  
214 Laboratory in the University of Liverpool. The apparatus is capable of applying confining  
215 pressures of up to 250 MPa and pore pressures up to 200 MPa. It measures ultra-low permeability  
216 down to  $10^{-22} \text{ m}^2$  and a sample volume change of  $0.1 \text{ mm}^3$ . The servo-controlled pore fluid system  
217 controls pore fluid pressure and serves as a high precision volumometer. This system can be used  
218 to measure permeability through various methods including the pulse transient technique (Brace  
219 et al., 1968) applied in this study to obtain values of permeability for the fault gouges at different  
220 confining pressures. The gouge powders were prepared by mixing 0.4 g of the sample with 0.5 mL  
221 of distilled water. The paste was then placed between two sintered discs with a known permeability  
222 of  $10^{-13} \text{ m}^2$ . The discs holding a cylindrical gouge layer approximately 1 mm high were placed within  
223 a PVC jacket and coupled with the sample assembly. Once the sample was inside the pressure  
224 vessel, the confining and pore pressure were progressively increased from a pore pressure value of  
225 5 MPa that was kept for all measurements and an initial confining pressure of 10 MPa. The  
226 confining pressure was progressively increased in 20 MPa intervals to obtain permeability  
227 measurements at 5, 20, 40, 60, 80, and 100 MPa effective pressure. The pressure was left to  
228 equilibrate after each pressure increase until no changes in either pore or confining pressure were  
229 observed. The samples were recovered after depressurization and carefully measured to determine  
230 the final sample thickness and calculate permeability values. The pulse transient technique imposes  
231 a 1 MPa pressure differential in the upstream reservoir and bases the calculations on how this  
232 pressure increase is transmitted through the gouge sample to determine permeability (Brace et al.,  
233 1968).

## 234 4. Results

### 235 4.1 SEM observations

#### 236 4.1.1 Naturally deformed fault rocks

##### 237 a. Smectite- and palygorskite-rich fault gouge

238 BSE-SEM observations of the fault gouge from the Galera town area show that the rock is  
239 composed of a very fine grain phyllosilicate-rich matrix that constitutes the majority of the rock  
240 and surrounds micron-size clasts of dolomite, orthoclase and quartz. Deformation features in the  
241 sample include the presence of bands of very fine grain minerals alternated with bands of coarser  
242 minerals that suggest cataclastic processes including grain rotation and grain size reduction (Fig. 2).  
243 The observed structural features of the sample include the alignment of platy clay minerals in an  
244 orientation similar to the shear direction, between  $135^\circ$  and  $180^\circ$  to the shear vector (Rutter et al.,  
245 1986), hereafter called the P-foliation after Logan et al. (1979). A set of shears that transect the P-  
246 foliation were also identified in the gouge and correspond with the definition of  $R_1$  (Riedel) shears  
247 according to Logan et al., (1979). The gouge also exhibits surfaces parallel to the shear zone and  
248 with the same sense of shear, here referred to as Y surfaces (Logan et al., 1979).

##### 249 b. Sepiolite-rich fault gouge

250 Low magnification BSE images of the sepiolite-rich fault gouge show a homogeneous gouge with  
251 very fine grain size sepiolite that constitutes the majority of the sample (Fig. 3a). Deformation  
252 features are observed in the larger grain size phases that show mica-delamination and broken and  
253 aligned grains (Fig. 3a), however due to the clay size of the matrix further examination is restricted.  
254 Secondary electron image using in-lens detector of the gouge matrix shows fibrous sepiolite  
255 crystals with mainly two preferred orientations perpendicular to each other forming the majority  
256 of the gouge matrix (Fig. 3b).

## 257 4.1.2 Experimentally deformed fault rocks

### 258 a. Smectite and palygorskite fault gouge material (wet deformation)

259 The examined gouge layers were recovered from the sliders. Samples retain some features related  
260 to the experimental assembly such as the grooved surface of the sliders (Fig. 4a). High deformation  
261 is visible towards the limit with the grooves, these type of shears have been described as boundary  
262 shears. The experimentally deformed layers show microstructural features previously described for  
263 clay-rich fault gouges (Rutter et al., 1986), such as P-foliation (Fig. 4b and c) and  $R_1$  shears, the  
264 deformation bands are markedly noticeable when affecting coarser grains of mica and dolomite.

### 265 b. Sepiolite fault gouge material (wet deformation)

266 Deformation microstructures in the experimentally deformed sepiolite-rich gouge are highly  
267 pronounced in mineral phases with bigger grain size, however clay mineral alignment is hard to  
268 define (Fig. 5). The artificial grooves in the gouge were lost during the impregnation due to the  
269 highly localized strain in the boundary shears (Fig. 5). Larger gypsum crystals are deformed in  
270 domino –type asymmetric boudinage (Fig. 5b, 5c), while larger mica crystals align and delaminate  
271 in favor of areas of localized shear (Fig. 5d, 5e). Dolomite crystals also appear highly fragmented  
272 due to the transection of  $R_1$  and P surfaces with trail development (Fig. 5f).

### 273 c. Smectite and palygorskite fault gouge material (dry deformation)

274 The experimentally deformed gouge closely resembles the deformation structures identified in the  
275 natural gouge such as the  $R_1$  shears, bands of clay minerals alternated with bands of bigger grain  
276 size (Fig. 6a to 6d). A view of the shear planes shows the polished slickenside surface and striae,  
277 resulting from the shear (Fig. 6e, 6f).

### 278 d. Sepiolite fault gouge material (dry deformation)

279 SEM examination of the deformed gouge shows similar deformation microstructures to that  
280 observed in the gouge deformed naturally and under wet conditions (Fig. 7). A high proportion of

281 small incipient shears that align in a similar direction are evident. These same shears have no  
282 evident connection between them (Fig. 7c). Figures 7d to 7f show the presence of a grid-like  
283 microfabric of the deformed gouge caused by the two main preferred orientations of sepiolite  
284 fibers. The two orientations of the fibers persist even towards the  $R_1$  shears and on the shear  
285 planes (Fig. 7e, 7f).

#### 286 **4.1.3 Summary of micro-scale observations**

287 In the naturally deformed rocks, grain orientation for the two materials studied differs significantly.  
288 The smectite- and palygorskite-rich gouge shows grain alignment with a series of parallel structures  
289 following similar orientations, on the other hand in the sepiolite-rich gouge it is noticeable the  
290 presence of two or more orientations of the fibers. Meanwhile, the differences for grain orientation  
291 identified in the two naturally deformed gouges studied remain noticeable in the experimentally  
292 deformed rocks, grain alignment in the smectite- and palygorskite-rich gouge and grid microfabric  
293 in the sepiolite-rich gouge. Finally, the presence of water during deformation does not develop any  
294 significant differences in grain orientation for either gouge, showing a similar resulting  
295 microstructure under both wet and dry conditions.

#### 296 **4.2 TEM observations**

##### 297 **4.2.1 Naturally deformed fault rocks**

###### 298 **a. Smectite and palygorskite fault rock**

299 The gouge has a matrix mainly composed of smectite, with minor amounts of palygorskite and  
300 illite. The general texture of the rock shows phyllosilicate alignment as well as elongated porosity  
301 parallel to the basal planes of the crystals (Fig. 8a). The abundant presence of smectite helps to  
302 coat the coarse grains to maintain the fluid texture observed at lower magnification (Fig. 8b). High-  
303 resolution images of the rock matrix in a smectite-rich area show parallel to sub-parallel lattice  
304 fringes of smectite, the (001) spacing of smectite is measured to be around 1.05 nm to 1.30 nm,

305 due to the variable collapsing of its interlayer space in areas of poor impregnation (Fig. 8c, 8d).  
306 Lattice fringes with spacing that vary from 2.00 to 2.30 nm were also observed within the smectite-  
307 rich matrix, which might correspond to mixed layer I/S with a variable degree of collapse (Fig.  
308 8d). The smectite crystals present broken and displaced lattice planes where the low crystallinity  
309 of the clay grains is indicated by the absence of packets of more than two or three layers that never  
310 achieve a thickness of more than 10 nm (Fig. 8c, 8d). This kind of texture, which has been  
311 frequently described in smectites from both authigenic (Krekeler et al., 2004) and sedimentary (e.g.  
312 Nieto et al, 2016) environments, is compatible with plastic processes, able to accommodate the  
313 strain without breaking of the crystals. Illite shows lattice fringes with 1.00 nm spacing and is the  
314 most crystalline phase on the basis of selected area electron diffraction (SAED) patterns, however  
315 illite crystals are embedded in smectite crystals with a similar orientation, which hinders the  
316 chemical analysis of a single phase (Fig. 8e). HR-images show crystals with diffuse regions  
317 consistent with the polysomes structures described by Krekeler et al. (2005) (Fig. 8f).

#### 318 **b. Sepiolite fault rock**

319 The general texture of the rock showed that the fibers have mainly three preferred orientations:  
320 orientations 1 and 2 have the c-axis (direction of the fiber) parallel to the imaged plane and are  
321 oriented almost perpendicular to each other; orientation 3 has the c-axis of the fibers oriented  
322 perpendicular to the imaged plane, showing a transversal section of the bundles that appear in the  
323 image as small polygons (Fig. 9). These three orientations constitute a three-dimensional grid-like  
324 microfabric of the rock. The rock matrix is composed of fiber-aggregates (bundles) with different  
325 sizes that vary from 1  $\mu\text{m}$  to 100 nm (Fig. 9). The lack of fiber orientation in the rock matrix  
326 creates a large number of triangular to polygonal voids in the rock distributed throughout the  
327 matrix (Fig. 9). SAED patterns in the matrix are difficult to obtain, however, it is possible to  
328 observe reflections representing the 110 spacing of sepiolite at approximately 1.23 nm (Fig. 9b  
329 inset).

330 FIB-cut-lamellae extracted from the red rectangle shown in Figure 3a allowed the identification of  
331 the general sense of deformation of the samples (Fig. 10a). Lamellae TEM observations show a  
332 consistent orientation for a set of feather-like structures that coincides with the general direction  
333 of shear of the sample (Fig. 10b, d and e). The feather structures show significant reduction of the  
334 grain size by bending and eventually breaking the fibers, creating an area of small oriented fibers  
335 that form the feather structure and are only recognizable at the TEM-scale (Fig. 10).

336 HR-TEM images show that the (110) lattice fringes in sepiolite crystals are continuous and no  
337 layer terminations were observed (Fig. 11). High-resolution images of the sepiolite crystals show  
338 lattice plane spacings that vary from 1.10 nm to 1.24 nm (Fig. 11). Some crystals (Fig. 11a) exhibit  
339 d-spacing closer to the ideal 1.20 and 1.21 nm. Meanwhile, other sepiolite crystals show progressive  
340 decrease of the d-spacing (Fig. 11b and 11c).

341 High-resolution images on single fibers in the naturally deformed sepiolite-rich samples showed  
342 multiple crystals with intermediate d-spacings between palygorskite and sepiolite showing a range  
343 of d-spacings from 1.03 nm to 1.18 nm (Fig. 12a). Furthermore, the images show crystals with d-  
344 spacings of 1.04 to 1.06 nm which correspond to the (110) plane of palygorskite. Crystal defects  
345 as dislocations were identified within these palygorskite crystals (Fig. 12b).

#### 346 **4.2.2 Experimentally deformed gouges**

##### 347 **a. Smectite and palygorskite fault gouge material (wet and dry deformation)**

348 Under wet conditions, low magnification images of the experimentally deformed gouge show two  
349 distinctively different textures of the rock (Fig. 13a). The first texture shows an oriented fabric  
350 constituted of laminar aggregates (Fig. 13b) that isolate the lenses of the second texture (Fig. 13a).  
351 Smectite and illite crystals constitute the matrix of texture 1 in the artificially fabricated gouge,  
352 these phyllosilicates are aligned on their basal planes, contrary to the initial random orientation of  
353 the crushed and powdered natural rock when placed on the sliders. Smectite spacing in these  
354 samples has been identified at around 1.02 nm and it is possible to recognize a number of

355 deformation features including delamination of the phyllosilicates and shearing of phases with  
356 larger grain size, such as gypsum (Fig. 13b).

357 The second texture exhibits a more homogeneous aspect without visible crystals or any particular  
358 fabric orientation (Fig. 13c). High-resolution observations show that the origin of the two textures  
359 relates to the type of phyllosilicate in the area. Texture 1 is composed of smectite and illite, while  
360 texture 2 is entirely composed of the fibrous palygorskite (Fig. 13c).

361 Samples deformed under the absence of water (dry deformation) show the same kind of phase  
362 segregation observed in the samples deformed under wet conditions (Fig. 14). Smectite-rich areas  
363 form sigmoidal structures and present large elongated pores that follow the orientation of the  
364 fluid-like deformation structure (Fig. 14a). SAED patterns are difficult to obtain for individual  
365 grains; however, the general SAED patterns in the matrix of both textures show significant  
366 differences confirming the segregation of mineral phases by habit. SAED pattern from areas rich  
367 in planar phyllosilicates are turbostratic, where the long axis represents d-spacings of 1.00 nm  
368 corresponding with the lattice spacing of the (001) plane of illite and possibly the collapsed  
369 smectite crystals, and the short axis represents d-spacings of 0.52 nm corresponding with the (003)  
370 plane of smectite (Fig. 14b inset).

#### 371 **b. Sepiolite fault gouge (wet and dry deformation)**

372 The general texture in the gouge deformed under wet conditions shows a continuous feather  
373 structure or kinks (Fig. 15a and b). High-resolution images show (110) planes of sepiolite crystals  
374 with different d-spacing, varying from 1.14 to 1.20 nm (Fig. 15c), this particular image with angular  
375 edges is possibly viewing the crystals along the [100] direction. The parallelogram-shaped minerals  
376 could be the result of a cross-section of rod mesocrystals that resemble open channel defects  
377 described by Krekeler and Guggenheim (2008).

378 Very few images were obtained from the gouge deformed under dry conditions. The lattice fringe  
379 spacing of the sepiolite crystals measured in this preparation was 1.14 nm.



### 380 4.3 Analytical Electron Microscopy

381 AEM analyses of single crystals from the two fault gouges in the Galera Fault Zone were collected  
382 to define the chemical compositions of sepiolite, palygorskite and smectite crystals and are  
383 presented in Figure 16 in the form of the main octahedral oxides to detect transitional  
384 compositions between sepiolite and palygorskite as well as between palygorskite and smectites.  
385 The fibrous samples plot continuously in all the compositional ranges discriminated in Suárez and  
386 García-Romero (2013), without major compositional gaps (Fig. 16). AEM analysis of smectite and  
387 palygorskite have great similitudes, palygorskite has a slightly higher Mg content than smectite,  
388 however the most significant feature to differentiate between them is their morphology.

389 In order to identify whether or not the origin of the smectites present within the fault plane are  
390 authigenic, 103 smectite crystals were analyzed including smectites collected from within the fault  
391 plane and smectites from the two principal lithologies in the sedimentary sequence of the wall  
392 rock. The chemical composition of the major octahedral cations in the smectite crystals are  
393 presented in Figure 17. For the full list of normalized chemical formulas see Supplementary  
394 information, Table 1.

395 Most of the smectites analyzed show a beidellite character. Smectites from the lutitic strata show  
396 a higher content of Fe, while those from the marly strata show a higher Al content. Smectites from  
397 the fault plane have chemical features similar to both the marls and the lutites from the wall rock,  
398 however their Mg content within the octahedral layer appears slightly higher than those from the  
399 wall rocks.

400 The identification of a small peak of palygorskite in XRD analysis (see the diffractograms of  
401 samples in Supplementary Fig. 1) motivated the exploration of the chemical composition of the  
402 sepiolite fibers in the sepiolite-rich gouge. A sequence of chemical analysis acquired within 46  
403 individual fibers of sepiolite show small content of aluminum in 16 of the crystals. The highest Al  
404 content appears towards the edges of the crystals in 9 of the 16 crystals; while for the remaining 7

405 the Al content seems to be similarly distributed along the crystals. Differences in the Al content  
406 are noticeable within an individual fiber (Fig. 18), where the area of analysis 3 (in red) shows  
407 significantly higher Al content than areas 1 and 2.

#### 408 **4.4 Permeability**

409 The values obtained from the permeability measurements on the smectite-rich fault gouge range  
410 between  $1 \times 10^{-20}$  to  $1 \times 10^{-21} \text{ m}^2$ , which decrease almost linearly with a rise in confining pressure  
411 from 5 to 100 MPa, while results for the sepiolite-rich fault gouge range between  $1 \times 10^{-18}$  to  $1 \times 10^{-19}$   
412  $\text{ m}^2$  (Fig. 19).

413

## 414 5. Discussion

### 415 5.1 Sepiolite to palygorskite phase transformation in the fault gouge

416 Sepiolite is the major phyllosilicate in the central segment of the Galera Fault (Sánchez-Roa et al.,  
417 2016), as is supported by low- and high-resolution TEM images (Figs. 9, 10, 11 and 12).  
418 Nevertheless, significant Al content has been found in various analyzed fibers, defining a  
419 continuous trend between the compositional fields of sepiolite and palygorskite (Fig. 16). This Al  
420 is preferentially associated to the border of the fibers, with a tendency to be absent in their centers  
421 (Fig. 18), and is expected to be associated to nanometer sized (less than 6 nm) discrete areas of  
422 palygorskite (Fig. 12b, 18). The d-spacing variation of lattice fringes on HR-TEM images of  
423 sepiolite ranges from 1.1 nm to 1.24 nm (Fig. 11). The presence of different d-spacings could  
424 suggest small contributions of palygorskite polysomes to the sepiolite structure (Suárez and  
425 García-Romero, 2013) that alter the regular (110) spacing of sepiolite ideally defined at 1.22 nm.  
426 The acquired images are consistent with this interpretation, however it is important to note that  
427 thickness, focus or beam damage effects could also cause alteration of regular spacings.

428 In nature, the progressive transformation from one phase to another, due to changes in chemical  
429 and/or physical conditions, may occur via polysomatic reactions or as growth of discrete crystals  
430 of the new phase. Polysomatic reactions are seen in the case of smectite to illite through  
431 illite/smectite mixed-layers (Hower et al., 1976), or in the case of the transformation from  
432 pyroxenes to amphiboles through pyriboles (Veblen and Buseck, 1981). In both of these cases,  
433 high-resolution images display the new polysome as individual unit cells within the former phase  
434 showing their respective characteristic spacings, which allow the clear identification of the areas in  
435 which the new polysome is present (Bozhilov et al., 2007; Vázquez et al., 2014). In other cases, the  
436 new phase nucleates as discrete crystals, sometimes assisted by topotactic or epitactic mechanisms  
437 (Sánchez-Navas, 1999), but without the existence of intermediate stages (e.g. chlorite to biotite  
438 transformation or the transformation among the aluminum silicate polymorphs). Figure 12 could

439 represent such a case or could be a more advanced stage in the progressive development of  
440 polysomes (Krekeler et al., 2005; Krekeler and Guggenheim, 2008). Contrary to the layer silicates,  
441 the sepiolite- palygorskite polysomes would be individual chains. Considering that a lattice fringe  
442 in a high-resolution image would include at least 15 unit cells in depth, when assuming an average  
443 width of 20 nm per lath, the variability in the measured spacings could be the result of different  
444 proportions of the two types of chains, representing a weighted average of the spacings of the two  
445 polysomes. Nevertheless, we have not found individual lattice fringes corresponding to the  
446 palygorskite spacing in a matrix of sepiolite, contrary to the case described for pyriboles by  
447 Bozhilov et al. (2007). Hence, our results cannot be considered conclusive in relation to the  
448 mechanism of transformation between sepiolite and palygorskite, however chemical analysis  
449 confirms that the Al content appears often towards the edges of the crystals (Fig. 18). This suggests  
450 that the phase transformation starts affecting the edges of sepiolite fibers by including Al in  
451 palygorskite polysomes or directly producing the growth of individual crystals of palygorskite. This  
452 phenomenon in the context of fault zones can be related to fluid-rock interactions of the gouge  
453 (Sánchez-Roa et al., 2016).

## 454 **5.2 Genetic relation between palygorskite and Mg-smectite in the fault gouge**

455 Quantitative chemical analysis in palygorskite and smectite particles show a compositional  
456 overlapping between fibrous and smectite crystals (Fig. 16). This chemical similarity of some  
457 palygorskite and smectite crystals suggests that either a transformation or some mineral epitaxial  
458 overgrowth between smectite and palygorskite crystals is taking place within the smectite- and  
459 palygorskite-rich sample (Fig. 16).

460 To explore this possibility, AEM analysis on 103 crystals of smectite from the two main levels of  
461 the sedimentary sequence of the wall rock and smectites from the fault plane are shown in Figure  
462 17. The results of the normalized chemical formula in the three groups of smectite show a higher  
463 interlayer Mg content for the smectites of the fault plane, but are inconclusive regarding a change

464 of the 2:1 layer composition of smectites. The most common products of the transformation of  
465 fibrous clay minerals in experimental studies are Mg-rich smectites (Golden and Dixon, 1990).  
466 This suggests that a portion of the smectites within the fault plane could have an authigenic origin,  
467 which would be the result of a transformation reaction from palygorskite (Krekeler et al., 2005),  
468 however the similarity of the 2:1 layer compositions between the smectites in the two contexts  
469 does not allow to either confirm nor deny such possibility.

470 Previous studies on the transformation of fibrous clay minerals to smectites have experimentally  
471 showed that the product of hydrothermally transformed sepiolite is often constituted by lath-like  
472 morphology smectite (Güven and Carney, 1979). This phenomenon was again observed in the  
473 transformation from palygorskite to smectite and explained by smectite forming within the  
474 palygorskite laths prior to their physical disruption producing a palygorskite pseudomorph  
475 composed of smectite (Golden and Dixon, 1990).

476 Based on the two well-defined textures in the experimentally deformed rock (Fig. 13, 14) and the  
477 absence of the texture segregation in the naturally deformed rock (Fig. 8), we suggest that this  
478 textural difference could be an indication that the palygorskite crystals were indeed intergrown  
479 with smectite crystals in the natural rock. Segregation of mineral phases observed in the  
480 experimentally deformed rocks can, on the other hand, occur as a result of the disaggregation of  
481 the rock during sample preparation and re-aggregation of crystals by habit during the experiment  
482 (Fig. 13).

### 483 **5.3 Deformation features in planar and fibrous clay minerals**

484 Clay minerals are major constituents of many fault gouges (Haines and van der Pluijm, 2012; Rutter  
485 et al., 2012; Schleicher et al., 2013), reaching up to 99.5% in the Central Deforming Zone of the  
486 San Andreas Fault (Hadizadeh et al., 2012; Janssen et al., 2014), and constitute the majority of the  
487 fault gouge in the Galera Fault Zone (Sánchez-Roa et al., 2016). However, not all clay minerals  
488 have the same physical and chemical properties and possibly nor the same mode of deformation.

489 In this section, we aim to compare the deformation features from platy and fibrous clay minerals  
490 to identify possible differences in their behavior under shear in both natural faults and friction  
491 experiments. The Galera Fault Zone is an ideal natural example for this study due to the presence  
492 of both platy and fibrous clay minerals within its main sliding planes (Sánchez-Roa et al., 2016).

493 Frictional deformation in phyllosilicates is facilitated by a series of micromechanisms including  
494 grain-grain sliding when the planar minerals are aligned on their basal planes, delamination,  
495 cataclasis, crystal plasticity, and pressure-solution creep. These processes are controlled by many  
496 factors including pressure and temperature (Beeler, 2007; French et al., 2015). SEM observations  
497 on samples in this study do not show significant differences between the microstructures of wet  
498 and dry frictional experiments as has been previously described for microstructures of  
499 phyllosilicates sheared at low temperatures (Moore and Lockner, 2004; Behnsen and Faulkner,  
500 2013; Haines et al., 2013). In general, all SEM observations in the experimentally deformed  
501 samples show distributed deformation within the phyllosilicates of the matrix (Figs. 2 to 7).

502 TEM observations on the smectite-rich gouge show how smectite crystals present broken and  
503 displaced lattice fringes in the rock matrix in order to accommodate deformation (Fig. 8). In this  
504 way smectite crystals ensure a uniform distribution of the shear in the rock. The quick alignment  
505 of the smectite and illite crystals of the matrix of the smectite- and palygorskite-rich samples in the  
506 experimentally deformed gouges demonstrate that when the shear deformation starts, the platy  
507 minerals rapidly adopt a preferred orientation producing a very similar fabric to the one observed  
508 in the naturally deformed rocks. Smectite crystals aggregate together with the same orientation on  
509 their basal planes, and facilitate grain on grain sliding as well as delamination processes that  
510 accommodate deformation through creeping (Fig. 8).

511 On the other hand, the fibrous phyllosilicate gouge shows mainly three different orientations of  
512 the fibers. This grid-like microfabric (Fig. 9) and the absence of weak cleavage planes for  
513 intragranular sliding result in the formation of feather structures that mark areas where the

514 deformation processes have been localized producing the observed grain size reduction through a  
515 mechanical bending and breaking of the fibers. The orientation of the feather-like structures  
516 (Fig. 10), resemble the orientation of Riedel shears (Rutter et al., 1986). Indicating that deformation  
517 is localizing by bending and breaking the fibers at a very small scale that is not visible until the clay  
518 fraction of the gouge is examined in detail (Fig. 10, 15).

519 In the case of the experimentally deformed smectite- and palygorskite-rich gouge no feather  
520 structures were observed, a phenomenon that can be explained by the high amount of smectite in  
521 the sample that accommodates most of the deformation without the need to affect the stronger  
522 palygorskite-rich areas.

523 In HR-TEM observations, the delamination processes are visible in the smectite crystals, however  
524 in the fibrous materials the lattice fringes appear continuous. The higher strength of the fibrous  
525 structure hinders delamination processes accommodating the imposed deformation by breaking  
526 and bending of fibers resulting in a series of feather-like structures at the micro-scale (Fig. 10).

#### 527 **5.4 Geological implications**

528 Based on our results, we propose that the mineral transformations in the Mg-rich fault gouges of  
529 the Galera Fault are a consequence of the fluid depletion in Mg with progressive exhumation and  
530 a proportional increase of Al content enhanced by the interaction with the Al-rich wall rocks.  
531 Sánchez-Roa et al. (2016) showed that mineralogical and geochemical differences between fault  
532 gouges and wall rocks are likely to be the result of periods of fluid-rock interaction within the  
533 Galera Fault. MgO and As gains in fault gouges pointed to a circulation of hot deep fluids as the  
534 source of the Mg-rich fluid, produced by the dissolution of the thick dolostone sequences that  
535 form the Mesozoic carbonatic basement. Sepiolite precipitated directly from a Mg-rich fluid while  
536 palygorskite and smectite formation could be products of the interaction of the fluid with the Al-  
537 rich host rock and the infiltration of oxidized basinal fluids with high pH<sup>+</sup>. The evolution sequence  
538 identified in this study starts with the precipitation of sepiolite from Mg-rich hydrothermal fluids

539 (Sánchez-Roa et al., 2016). Sepiolite crystals start to incorporate palygorskite domains to produce  
540 a first evolution stage where both sepiolite and palygorskite are present as independent crystals as  
541 is the case of the studied gouge from the Galera Fault. Following this, we propose a second  
542 evolution stage intermediate between the two gouges studied, in which sepiolite has been  
543 transformed to palygorskite. The smectite-palygorskite gouge from the Galera Fault constitutes a  
544 third stage of transformation, in which the smectites in the wall rock change their interlayer  
545 composition and a part of the palygorskite could have been transformed to smectite as a result of  
546 the large Al-availability forming Mg-rich smectite. In a more advanced stage, it is possible that  
547 further alteration of the fault gouge results in a platy Mg-rich smectite enrichment, which could  
548 alter fault strength and permeability, affecting earthquake nucleation and propagation processes.

549 The permeability of fault zones is a relevant property that controls the subsurface fluid flow and  
550 plays an important role in coseismic fluid pressure changes, pore pressure build-ups and potential  
551 weakening of faults (Scuderi and Collettini, 2016; Faulkner et al., 2018). There is a difference of  
552 almost two orders of magnitude in the measured permeability for the two fault gouges in this  
553 study (Fig. 19). This permeability contrast can be related to the dominant phyllosilicate for each  
554 gouge. Both gouges decrease their permeability with increasing confining pressure, however the  
555 smectite-rich fault gouge sustains greater decline in permeability for a given change in confining  
556 pressure (Fig. 19). The faster decrease in permeability for the smectite-gouge can be related to a  
557 much higher level of sheet alignment and lateral connectivity of the platy smectite crystals at  
558 medium to high pressures facilitated by the high particle mobility of this mineral (Behnsen and  
559 Faulkner, 2011). On the other hand, the grid-like microfabric in the fully fibrous material can leave  
560 room for a higher number of interconnected pores due to the lack of fiber alignment that adds to  
561 the structural microporosity of the fibers, as a consequence of their internal channels. These results  
562 show how the permeability of the gouges in the Galera Fault is strongly affected by the mineralogy  
563 of the gouge, implying that mineral authigenic growth and mineral transformations could  
564 constitute a controlling factor on the permeability of the fault zone.



565 The strength of the two fault gouges in the Galera Fault show highly contrasting values, the  
566 sepiolite-rich gouge has a higher friction coefficient ( $\mu=0.47$  under wet deformation), while the  
567 smectite and palygorskite-rich gouge has a significantly lower friction coefficient ( $\mu=0.17$  under  
568 wet deformation) (Sánchez-Roa et al., 2016). The presence of smectite has proven to have  
569 important effects on the strength of faults by contributing to a lower frictional strength and has  
570 been reported to have a weakening effect on concentrations as low as 10 wt% (Oohashi et al.,  
571 2015). Furthermore, previous studies comparing the strength of monomineralic fibrous clay  
572 minerals and the smectite saponite have shown that their frictional strength is dictated by their  
573 crystal structure showing that fibrous Mg-rich phyllosilicates are stronger than the platy smectite  
574 (Sánchez-Roa et al., 2017). Therefore, we suggest that the strength of the Galera Fault could be  
575 significantly controlled by the palygorskite to smectite ratio within the fault planes.

576 Mineral transformations between fibrous and planar clay minerals (specifically smectite) could  
577 occur in a variety of geological settings involving Mg-rich environments. As a consequence, these  
578 mineral transformations will considerably change important chemical and physical properties, such  
579 as surface area and cation exchange capacity that significantly alter the microfabric, permeability  
580 and strength of the geological material.

581

## 582 **Acknowledgments**

583 The authors would like to thank Dr. M.M. Abad-Ortega, A. Martínez-Morales, Dr. M. A. Laguna,  
584 Dr. A. Ibarra and Dr. R. Fernández-Pacheco for their support in electron microscopy data  
585 acquisition. The authors thank the reviewers E. García-Romero and M. Krekeler for their  
586 comments that led to significant improvements. This work has been financed by the research  
587 projects CGL2011-30153-C02-01, CGL2011-30153- C02-02, and CGL2013-46169-C2-1-P from  
588 MINECO, research project UJA2014/06/17 from the Universidad-Caja Rural de Jaén, Research

589 Groups RNM-179 and RNM-325 of the Junta de Andalucía, UK NERC grant NE/J024449/1  
590 and the F.P.I. Grant No. BES-2012-052 562 from the Spanish Government (Ministerio de  
591 Economía y Competitividad).

## 592 **References**

593 Abad, I., Nieto, F., and Velilla, N., 2002, Chemical and textural characterisation of diagenetic to  
594 low-grade metamorphic phyllosilicates in turbidite sandstones of the South Portuguese Zone:  
595 A comparison between metapelites and sandstones: *Schweizerische Mineralogische und*  
596 *Petrographische Mitteilungen*, v. 82, p. 303–324.

597 Beeler, N.M., 2007, Laboratory-observed faulting in Intrinsically and Apparently Weak Materials:  
598 *The Seismogenic Zone of Subduction Thrust Faults*, p. 370–449.

599 Behnsen, J., and Faulkner, D.R., 2013, Permeability and frictional strength of cation-exchanged  
600 montmorillonite: *Journal of Geophysical Research: Solid Earth*, v. 118, no. 6, p. 2788–2798,  
601 doi: 10.1002/jgrb.50226.

602 Behnsen, J., and Faulkner, D.R., 2011, Water and argon permeability of phyllosilicate powders  
603 under medium to high pressure: *Journal of Geophysical Research: Solid Earth*, v. 116, no.  
604 12, p. 1–13, doi: 10.1029/2011JB008600.

605 Bozhilov, K.N., Brownstein, D., and Jenkins, D.M., 2007, Biopyribole evolution during tremolite  
606 synthesis from dolomite and quartz in CO<sub>2</sub>-H<sub>2</sub>O fluid: *American Mineralogist*, v. 92, no. 5-  
607 6, p. 898–908, doi: 10.2138/am.2007.2376.

608 Brace, W.F., Walsh, J.B., and Frangos, W.T., 1968, Permeability of Granite under High Pressure:  
609 *Journal of Geophysical Research*, v. 73, no. 6.

- 610 Cliff, G. and Lorimer, G. W., 1975, The quantitative analysis of thin specimens: *Journal of*  
611 *Microscopy*, 103: 203-207. doi:10.1111/j.1365-2818.1975.tb03895.x
- 612 Cox, S.F., Knackstedt, M.A., and Braun, J., 2001, Principles of structural control on permeability  
613 and fluid flow in hydrothermal systems: *Reviews in Economic Geology*, v. 14, p. 1–24.
- 614 Faulkner, D.R., Jackson, C.A.L., Lunn, R.J., Schlische, R.W., Shipton, Z.K., Wibberley, C.A.J., and  
615 Withjack, M.O., 2010, A review of recent developments concerning the structure, mechanics  
616 and fluid flow properties of fault zones: *Journal of Structural Geology*, v. 32, no. 11, p. 1557–  
617 1575, doi: 10.1016/j.jsg.2010.06.009.
- 618 Faulkner, D.R., Sánchez-Roa, C., Boulton, C., and den Hartog, S.A.M., Pore Fluid Pressure  
619 Development in Compacting Fault Gouge in Theory, Experiments, and Nature: *Journal of*  
620 *Geophysical Research: Solid Earth*, 123. <https://doi.org/10.1002/2017JB015130>
- 621 French, M.E., Chester, F.M., and Chester, J.S., 2015, Micromechanisms of creep in clay-rich gouge  
622 from the Central Deforming Zone of the San Andreas Fault: *Journal of Geophysical*  
623 *Research B: Solid Earth*, v. 120, no. 2, p. 827–849, doi: 10.1002/2014JB011496.
- 624 García-Romero, E., and Suárez, M., 2010, On the chemical composition of sepiolite and  
625 palygorskite: *Clays and Clay Minerals*, v. 58, no. 1, p. 1–20, doi:  
626 10.1346/CCMN.2010.0580101.
- 627 García-Romero, E., and Suárez, M., 2013, Sepiolite-palygorskite: Textural study and genetic  
628 considerations: *Applied Clay Science*, doi: 10.1016/j.clay.2013.09.013.
- 629 García-Tortosa, F.J., Alfaro, P., Sanz de Galdeano, C., and Galindo-Zaldívar, J., 2011, Glacis  
630 geometry as a geomorphic marker of recent tectonics: The Guadix-Baza basin (South Spain):  
631 *Geomorphology*, v. 125, no. 4, p. 517–529, doi: 10.1016/j.geomorph.2010.10.021.

- 632 Giese, R.F., 1978, Electrostatic Interlayer Forces of Layer Structure Minerals.: Clays and Clay  
633 Minerals, v. 26, no. 1, p. 51–57, doi: 10.1346/CCMN.1978.0260106.
- 634 Golden, D.C., and Dixon, J.B., 1990, Low-temperature alteration of palygorskite to smectite: v.  
635 38, no. 4, p. 401–408.
- 636 Guven, N., and Carney, L.L., 1979, Hydrothermal Transformation of Sepiolite to Stevensite and  
637 The Effect of Added Chlorides and Hydroxides.: Clays and Clay Minerals, v. 27, no. 4, p.  
638 253–260, doi: 10.1346/CCMN.1979.0270403.
- 639 Hadizadeh, J., Mitterpergher, S., Gratier, J.P., Renard, F., Di Toro, G., Richard, J., and Babaie, H.  
640 a., 2012, A microstructural study of fault rocks from the SAFOD: Implications for the  
641 deformation mechanisms and strength of the creeping segment of the San Andreas Fault:  
642 Journal of Structural Geology, v. 42, p. 246–260, doi: 10.1016/j.jsg.2012.04.011.
- 643 Haines, S.H., Kaproth, B., Marone, C., Saffer, D., and Van der Pluijm, B., 2013, Shear zones in  
644 clay-rich fault gouge: A laboratory study of fabric development and evolution: Journal of  
645 Structural Geology, v. 51, p. 206–225, doi: 10.1016/j.jsg.2013.01.002.
- 646 Haines, S.H., and van der Pluijm, B.A., 2012, Patterns of mineral transformations in clay gouge,  
647 with examples from low-angle normal fault rocks in the western USA: Journal of Structural  
648 Geology, v. 43, p. 2–32, doi: 10.1016/j.jsg.2012.05.004.
- 649 Hickman, S., Sibson, R., and Bruhn, R., 1995, Mechanical involvement of fluids in faulting: Journal  
650 of Geophysical Research, v. 100, no. B7, p. 12831–12840, doi: 10.1029/94EO01059.
- 651 Houwers, M.E., Heijnen, L.J., Becker, A., and Rijkers, R., 2015, A Workflow for the Estimation  
652 of Fault Zone Permeability for Geothermal Production A General Model Applied on the

- 653 Roer Valley Graben in the Netherlands: Proceedings World Geothermal Congress 2015, , no.  
654 April, p. 9.
- 655 Hower, J., Eslinger, E. V., Hower, M.E., and Perry, E. a., 1976, Mechanism of burial  
656 metamorphism of argillaceous sediment: Geological Society Of America Bulletin, v. 87, no.  
657 60512, p. 725–737, doi: 10.1130/0016-7606(1976)87<725.
- 658 Ibanez, W.D., and Kronenberg, A.K., 1993, Experimental deformation of shale: Mechanical  
659 properties and microstructural indicators of mechanisms: International Journal of Rock  
660 Mechanics and Mining Sciences and, v. 30, no. 7, p. 723–734, doi: 10.1016/0148-  
661 9062(93)90014-5.
- 662 Janssen, C., Wirth, R., Wenk, H.R., Morales, L., Naumann, R., Kienast, M., Song, S.R., and Dresen,  
663 G., 2014, Faulting processes in active faults - Evidences from TCDP and SAFOD drill core  
664 samples: Journal of Structural Geology, v. 65, p. 100–116, doi: 10.1016/j.jsg.2014.04.004.
- 665 Kim, J.W., Peacor, D.R., Tessier, D., and Elsass, F., 1995, A technique for maintaining texture and  
666 permanent expansion of smectite interlayers for TEM observations: Clays and Clay Minerals,  
667 v. 43, no. 1, p. 51–57, doi: 10.1346/CCMN.1995.0430106.
- 668 Krekeler, M.P.S., Guggenheim, S., Rakovan, J., 2004, A microtexture study of palygorskite-rich sediments  
669 from the Hawthorne Formation, Southern Georgia, by transmission electron microscopy and atomic force  
670 microscopy. Clays and Clay Minerals, v. 52, no. 3, p. 263–274.
- 671 Krekeler, M.P.S., Hammerly, E., Rakovan, J., Guggenheim, S., 2005, Microscopy studies of the  
672 palygorskite to smectite transformation. Clays and Clay Minerals, 53, 94–101.

- 673 Krekeler, M.P.S., and Guggenheim, S., 2008, Defects in microstructure in palygorskite-sepiolite  
674 minerals: A transmission electron microscopy (TEM) study: Applied Clay Science, v. 39, no.  
675 1-2, p. 98–105, doi: 10.1016/j.clay.2007.05.001.
- 676 Logan, J.M., Friedman, M., Higgs, N., Dengo, C., and Shimamoto, T., 1979, Experimental studies  
677 of simulated gouge and their application to studies of natural fault zones: Proc. Conf. VIII -  
678 Analysis of Actual Fault Zones in Bedrock, p. 305–343.
- 679 Mares, V.M., and Kronenberg, a. K., 1993, Experimental deformation of muscovite: Journal of  
680 Structural Geology, v. 15, no. 9-10, p. 1061–1075, doi: 10.1016/0191-8141(93)90156-5.
- 681 Mitchell, T.M., and Faulkner, D.R., 2008, Experimental measurements of permeability evolution  
682 during triaxial compression of initially intact crystalline rocks and implications for fluid flow  
683 in fault zones: Journal of Geophysical Research: Solid Earth, v. 113, no. 11, p. 1–16, doi:  
684 10.1029/2008JB005588.
- 685 Moore, D.E., and Lockner, D.A., 2004, Crystallographic controls on the frictional behavior of dry  
686 and water-saturated sheet structure minerals: Journal of Geophysical Research, v. 109, no.  
687 B03401, p. 1–16, doi: 10.1029/2003JB002582.
- 688 Nieto, F., Arroyo, X., Aróstegui, J., 2016, XRD-TEM-AEM comparative study of *n*-  
689 alkylammonium smectites and interstratified minerals in shallow-diagenetic carbonate  
690 sediments of the Basque-Cantabrian Basin: American Mineralogist, v. 101, p. 385–398, doi:  
691 <https://doi.org/10.2138/am-2016-5301>.
- 692 Oohashi, K., Hirose, T., Takahashi, M., and Tanikawa, W., 2015, Dynamic weakening of smectite-  
693 bearing faults at intermediate velocities: Implications for subduction zone earthquakes:  
694 Journal of Geophysical Research-Solid Earth, v. 120, p. 11881, doi:  
695 10.1002/2015JB011881.Received.

- 696 Overwijk, M.H.F., 1993, Novel scheme for the preparation of transmission electron microscopy  
697 specimens with a focused ion beam: *Journal of Vacuum Science & Technology B: Microelectronics and Nanometer Structures*, v. 11, no. 6, p. 2021–2024, doi:  
698 10.1116/1.586537.
- 700 Peacor, D.R., 1992, Analytical electron microscopy, *in* Buseck, P.R. ed., *Minerals and reactions at*  
701 *the atomic scale: Transmission electron microscopy*, Mineralogical Society of America, p.  
702 113–140.
- 703 Rutter, E.H., Faulkner, D.R., and Burgess, R., 2012, Structure and geological history of the  
704 Carboneras Fault Zone, SE Spain: Part of a stretching transform fault system: *Journal of*  
705 *Structural Geology*, v. 45, p. 68–86, doi: 10.1016/j.jsg.2012.08.009.
- 706 Rutter, E.H., Maddock, R.H., Hall, S.H., and White, S.H., 1986, Comparative microstructures of  
707 natural and experimentally produced clay-bearing fault gouges: *Pure and Applied Geophysics*,  
708 v. 124, no. 1-2, p. 3–30, doi: 10.1007/BF00875717.
- 709 Sakuma, H., and Suehara, S., 2015, Interlayer bonding energy of layered minerals: Implication for  
710 the relationship with friction coefficient: *Journal of Geophysical Research: Solid Earth*, p.  
711 2212–2219, doi: 10.1002/2015JB011900.
- 712 Sánchez-Navas, A., 1999, Sequential kinetics of a muscovite-out reaction: A natural example:  
713 *American Mineralogist*, v. 84, no. 9, p. 1270–1286.
- 714 Sánchez-Navas, A., and Galindo-Zaldívar, J., 1993, Alteration and deformation microstructures of  
715 biotite from plagioclase-rich dykes (Ronda Massif, S. Spain): *European Journal of Mineralogy*,  
716 v. 5, no. 1987, p. 245–256.

- 717 Sánchez-Roa, C., Jiménez-Millán, J., Abad, I., Faulkner, D.R., Nieto, F., and García-Tortosa, F.J.,  
718 2016, Fibrous clay mineral authigenesis induced by fluid-rock interaction in the Galera fault  
719 zone (Betic Cordillera, SE Spain) and its influence on fault gouge frictional properties:  
720 Applied Clay Science, doi: 10.1016/j.clay.2016.06.023.
- 721 Sánchez-Roa, C., Faulkner, D.R., Boulton, C., Jimenez-Millan, J., Nieto, 2017, How phyllosilicate  
722 mineral structure affects fault strength in Mg-rich fault systems: Geophysical Research  
723 Letters, doi:
- 724 Schleicher, A.M., Hofmann, H., and van der Pluijm, B.A., 2013, Constraining clay hydration state  
725 and its role in active fault systems: Geochemistry, Geophysics, Geosystems, v. 14, no. 4, p.  
726 1039–1052, doi: 10.1002/ggge.20077.
- 727 Schleicher, A.M., Van Der Pluijm, B. a., Solum, J.G., and Warr, L.N., 2006, Origin and significance  
728 of clay-coated fractures in mudrock fragments of the SAFOD borehole (Parkfield,  
729 California): Geophysical Research Letters, v. 33, no. 16, doi: 10.1029/2006GL026505.
- 730 Schleicher, A.M., van der Pluijm, B.A., and Warr, L.N., 2012, Chlorite-smectite clay minerals and  
731 fault behavior: New evidence from the San Andreas Fault Observatory at Depth (SAFOD)  
732 core: Lithosphere, v. 4, no. 3, p. 209–220, doi: 10.1130/L158.1.
- 733 Scuderi, M.M., and Collettini, C., 2016, The role of fluid pressure in induced vs. triggered  
734 seismicity: insights from rock deformation experiments on carbonates.: Scientific reports, v.  
735 6, no. April, p. 24852, doi: 10.1038/srep24852.
- 736 Sibson, R.H., White, S.H., and Atkinson, B.K., 1979, Fault rock distribution and structure within  
737 the Alpine Fault Zone: a preliminary account, in The Origin of the Southern Alps, R. I.  
738 Walcott and M. M. Cresswell (Editors), R. Soc. New Zealand Bull. 18, 55–65.



- 739 Suárez, M., and García-Romero, E., 2013, Sepiolite–palygorskite: a continuous polysomatic series.  
740 Clays Clay Miner. 61, 5, 461–472.
- 741 Van der Pluijm, B., Lee, J., and Peacor, D.R., 1988, Analytical Electron Microscopy and the  
742 Problem of Potassium Diffusion: Clays and Clay Minerals, v. 36, no. 6, p. 498–504.
- 743 Vázquez, M., Nieto, F., Morata, D., Droguett, B., Carrillo-Rosua, F.J., and Morales, S., 2014,  
744 Evolution of clay mineral assemblages in the Tinguiririca geothermal field, Andean Cordillera  
745 of central Chile: an XRD and HRTEM-AEM study: Journal of Volcanology and Geothermal  
746 Research, v. 282, p. 43–59, doi: 10.1016/j.jvolgeores.2014.05.022.
- 747 Veblen, D.R., and Buseck, P.R., 1981, Hydrous pyriboles and sheet silicates in pyroxenes and  
748 uralites: intergrowth microstructures and reaction mechanisms.: American Mineralogist, v.  
749 66, no. 11-12, p. 1107–1134.
- 750 Whitney, D.L., and Evans, B.W., 2010, Abbreviations for names of rock-forming minerals.  
751 American Mineralogist, 95, 185–187.

752 **Figure Captions**

753 **Figure 1.** Geological map of the Galera Fault, modified from García-Tortosa et al. (2011). I:  
754 Sampling site by the Galera Village, Smectite- and palygorskite-rich fault gouge II: Sampling site  
755 Rambla de los Pílares, Sepiolite-rich fault gouge.

756 **Figure 2.** BSE image showing the deformation features of the naturally deformed smectite and  
757 palygorskite fault gouge, including P-foliation following the alignment of platy clay minerals, R<sub>1</sub>  
758 (Riedel) shears transecting the P-foliation, and Y surfaces parallel to the shear zone. Mineral  
759 abbreviations according to Whitney and Evans (2010), Or: orthoclase, Dol: dolomite, Qz: quartz.

760 **Figure 3. a.** BSE image showing the deformation features of the naturally deformed sepiolite fault  
761 gouge and deformation in larger grains of mica and dolomite. The red rectangle indicates the area  
762 selected for FIB-SEM lamellae extraction for TEM analysis **b.** Secondary electron image (in-lens  
763 detector) of the matrix of the rock showing the fibrous character of sepiolite.

764 **Figure 4. a.** BSE image of the experimentally deformed smectite and palygorskite fault gouge  
765 material under wet deformation. **b.** Enlarged view of the R<sub>1</sub> shear and P-foliation. **c.** Enlarged  
766 view of the P-foliation and alignment of dolomite and orthoclase grains.

767 **Figure 5. a.** BSE image of the experimentally deformed sepiolite fault gouge material under wet  
768 deformation. Shear direction indicated with half arrows. **b.** Enlargement of a boudinage structure  
769 on a gypsum crystal. **c** Enlargement of R<sub>1</sub> shear. Shear direction indicated with half arrows. **d to f.**  
770 Enlargement of structural features in the sample.

771 **Figure 6. a.** BSE image of the experimentally deformed smectite and palygorskite fault gouge  
772 material under dry deformation. **b, c, and d.** Enlargement of structural features in the sample.  
773 The red rectangle indicates the area selected for FIB-SEM lamellae extraction for TEM analysis **e.**

774 and **f.** Secondary electrons image of the shear planes after deformation with horizontal striae and  
775 polished slickenside surface.

776 **Figure 7. a.** BSE image of the experimentally deformed sepiolite fault gouge material under dry  
777 deformation. **b and c.** Enlargement of structural features in the sample. The red parallelogram  
778 indicates the site selected for FIB-SEM extraction for TEM analysis. **d.** Secondary electrons high-  
779 magnification image (in-lens detector) showing sepiolite crystals of the matrix **e.** and **f.** Secondary  
780 electrons image of the shear planes after deformation under dry conditions.

781 **Figure 8. a.** TEM image showing the general texture of the naturally deformed smectite and  
782 palygorskite fault rock. **b.** Smectite crystals coating coarse dolomite grain. **c.** High-resolution image  
783 of smectite crystals showing broken and displaced lattice fringes. **d.** Smectite-rich matrix shows  
784 smectite crystals with (001) spacing of 1.30 nm, and an area of unidentified phases with lattice  
785 fringes spaced 2.00 to 2.30 nm. **e.** HR-image of the matrix of the rock showing the proximity of  
786 the smectite and illite crystals. **f.** HR-image of crystals with discontinuous lattice fringes of variable  
787 d-spacing ranging from 1.9 to 2.4 nm. Mineral abbreviations according to Whitney and Evans  
788 (2010), Ill: illite, Dol: dolomite, Sme: smectite.

789 **Figure 9.** TEM images from a Cu-washer of the sepiolite fault rock. **a.** General fabric on the rock  
790 with variable rod sizes. **b.** Image of the rock matrix showing the disorientation of sepiolite fibers.  
791 Inset: SAED pattern on the rock matrix. Mineral abbreviations according to Whitney and Evans  
792 (2010), Sep: sepiolite.

793 **Figure 10.** TEM images of a FIB-lamellae sample of a sepiolite fault rock **a.** General view of the  
794 lamellae extracted from the red rectangle shown in Fig. 3a. Small letters show the position of  
795 subfigures b, d and e within the extracted FIB-lamellae. Arrows indicate the direction of shear. **b.**  
796 Feather structure following the direction of shear. **c.** General texture of the naturally deformed

797 sepiolite-rich fault rock. **d. and e.** Feather structures. Mineral abbreviations according to Whitney  
798 and Evans (2010), Sep: sepiolite.

799 **Figure 11. a.** High-resolution TEM image of the sepiolite crystal lattice with close to ideal d-  
800 spacing 1.21 nm. Insets show the intensity profiles along crystals A and B and average d-spacing  
801 results. **b and c.** High-resolution images of the sepiolite crystal lattice with variable d-spacing from  
802 1.10 nm to 1.24 nm. Mineral abbreviations according to Whitney and Evans (2010), Sep: sepiolite.

803 **Figure 12.** HR-TEM images of individual fibers in the sepiolite-rich gouge. **a.** Fibers with lattice  
804 spacing of 1.18 nm, slightly lower to those for ideal sepiolite. **b.** Fiber with lattice spacings  
805 corresponding with a palygorskite crystal.

806 **Figure 13. a.** Low magnification image of the experimentally deformed smectite and palygorskite  
807 gouge exhibiting two distinctively different textures of the rock. **b.** Magnification of texture 1  
808 showing aggregates of smectite crystals. **c.** Magnification of texture 2 showing disoriented  
809 palygorskite fibers. Mineral abbreviations according to Whitney and Evans (2010), Gp: gypsum, Ill:  
810 illite, Pal: palygorskite, Sme: smectite.

811 **Figure 14. a.** TEM image and general view of the lamellae extracted from the red rectangle shown  
812 in Fig. 7c **b.** Magnification of texture 1 showing aggregates of smectite crystals. **inset.** SAED  
813 patterns of texture 1. **c.** Magnification of texture 2 showing disoriented palygorskite fibers. **inset.**  
814 SAED patterns of texture 2. Mineral abbreviations according to Whitney and Evans (2010), Pal:  
815 palygorskite, Sme: smectite.

816 **Figure 15. a.** Low magnification TEM image showing the general texture of the sepiolite fault  
817 gouge under wet deformation and kinked sepiolite laths **b.** TEM image on the feather-like  
818 structures that form the matrix after deformation **c.** HR-TEM image of sepiolite crystals in the  
819 sepiolite fault gouge material under wet deformation. Mineral abbreviations according to Whitney  
820 and Evans (2010), Sep: sepiolite.

821 **Figure 16.** Variability in the octahedral cation content of the sepiolites, palygorskites and smectites  
822 of the study and their chemical classification according to Suárez and García-Romero (2013). Ideal  
823 octahedral cation oxide content for sepiolite and palygorskite are plotted according to García-  
824 Romero and Suárez (2010).

825 **Figure 17.** Ternary plot of major octahedral cations in smectite crystals from the fault rock in blue,  
826 lutitic wall rock in red and marly wall rock in green. Yellow and light-blue squares correspond to  
827 smectite crystals from the fault plane analysed after homoionization with K and Ca respectively.

828 **Figure 18. a.** Sepiolite crystal and selected areas for microanalysis **b.** TEM-AEM analysis of three  
829 selected areas of sepiolite crystal.

830 **Figure 19.** Permeability measurements on the two gouges with increasing confining pressure on  
831 a triaxial deformation apparatus.

832

833

834 **Supplementary Material**

835 **Supplementary Table 1.** Structural formulas calculated from AEM data for smectites normalized to O<sub>10</sub>(OH)<sub>2</sub>. All

836 Fe as Fe<sup>3+</sup> and <sup>IV</sup>Al = (4 – Si).

	Sample	Formula											
		Si	AlIV	AlVI	Fe	Mg (oct)	Σ oct.	Ca	K	Na	Mg (inter)	Σ inter.	
Untreated samples	Fault gouge	1 GP-3-1	3.890	0.110	0.752	0.563	0.685	2.000	0.000	0.299	0.000	0.248	0.547
		2 GP-3-3	3.913	0.087	0.918	0.529	0.553	2.000	0.000	0.264	0.000	0.187	0.452
		3 GP-3-4	3.844	0.156	1.225	0.384	0.391	2.000	0.017	0.384	0.000	0.064	0.465
		4 GP-3-5	3.896	0.104	1.374	0.278	0.348	2.000	0.035	0.313	0.000	0.035	0.383
		5 GP-3-6	3.757	0.243	1.409	0.313	0.278	2.000	0.087	0.313	0.000	0.017	0.417
		6 GP-3-7	3.786	0.214	1.391	0.331	0.278	2.000	0.052	0.314	0.000	0.036	0.403
		7 GP-3-8	3.956	0.044	1.240	0.295	0.465	2.000	0.104	0.260	0.000	0.021	0.385
		8 GP-3-9	3.806	0.194	1.092	0.539	0.370	2.000	0.000	0.156	0.000	0.204	0.360
		9 GP-3-10	3.783	0.217	1.038	0.540	0.422	2.000	0.087	0.192	0.000	0.136	0.415
		10 GP-3-11	3.876	0.124	1.011	0.541	0.419	1.971	0.157	0.314	0.000	0.000	0.471
		11 GP-3-12	3.865	0.135	1.159	0.385	0.000	1.544	0.192	0.420	0.000	0.000	0.612
		12 GP-3-13	3.984	0.016	1.180	0.398	0.422	2.000	0.069	0.139	0.000	0.080	0.288
		13 GP-3-14	3.716	0.284	1.329	0.280	0.390	2.000	0.053	0.333	0.000	0.118	0.504
		14 GP-3-15	3.708	0.292	1.113	0.492	0.395	2.000	0.053	0.457	0.000	0.062	0.572
		15 GP-3-16	3.728	0.272	1.260	0.401	0.339	2.000	0.070	0.279	0.000	0.097	0.445
		16 GP-3-17	3.780	0.220	1.181	0.473	0.347	2.000	0.035	0.385	0.000	0.056	0.476
		17 GP-3-18	3.869	0.131	1.118	0.503	0.379	2.000	0.000	0.260	0.000	0.125	0.385
		18 GP-3-19	3.997	0.003	1.057	0.365	0.578	2.000	0.035	0.174	0.000	0.169	0.378
		19 GP-3-20	3.754	0.246	1.256	0.419	0.325	2.000	0.017	0.384	0.000	0.076	0.478
		20 GP-3-21	3.874	0.126	1.049	0.491	0.461	2.000	0.000	0.456	0.000	0.065	0.521
		21 GP-3-22	4.005	0.000	1.214	0.312	0.474	2.000	0.000	0.191	0.000	0.132	0.323
		22 GP-3-23	3.841	0.159	1.133	0.402	0.465	2.000	0.122	0.297	0.000	0.041	0.460
		23 GP-3-24	3.755	0.245	1.095	0.511	0.388	1.994	0.071	0.511	0.000	0.000	0.582
		24 GP-3-25	3.830	0.170	1.124	0.455	0.421	2.000	0.052	0.280	0.000	0.103	0.436
		25 GP-3-26	3.673	0.327	1.307	0.334	0.359	2.000	0.070	0.387	0.000	0.080	0.537
		26 GP-3-1	3.904	0.096	1.153	0.416	0.431	2.000	0.069	0.208	0.000	0.090	0.368
		27 GP-3-2	3.860	0.140	1.088	0.421	0.491	2.000	0.070	0.491	0.000	0.000	0.561
		28 GP-3-3	3.880	0.120	0.989	0.589	0.422	2.000	0.000	0.139	0.000	0.202	0.340
		29 GP-3-4	4.071	0.000	0.699	0.437	0.864	2.000	0.000	0.175	0.000	0.202	0.376
		30 GP-3-5	3.841	0.159	1.221	0.279	0.500	2.000	0.000	0.192	0.000	0.233	0.425
		31 GP-3-6	3.606	0.394	1.452	0.261	0.287	2.000	0.035	0.279	0.000	0.166	0.480
		32 GP-3-7	4.033	0.000	1.004	0.589	0.398	1.991	0.000	0.294	0.000	0.000	0.294
		33 GP-3-8	3.759	0.241	1.187	0.400	0.413	2.000	0.000	0.191	0.000	0.231	0.422
		34 GP-3-9	3.724	0.276	1.595	0.225	0.180	2.000	0.052	0.191	0.000	0.080	0.323
		35 GP-3-10	3.979	0.021	1.283	0.191	0.526	2.000	0.000	0.174	0.000	0.186	0.360
		36 GP-3-1	3.783	0.217	1.317	0.331	0.352	2.000	0.035	0.331	0.000	0.084	0.450
		37 GP-3-2	3.534	0.466	1.390	0.247	0.000	1.637	0.247	0.495	0.000	0.000	0.742
		38 GP-3-3	3.722	0.278	1.242	0.454	0.303	2.000	0.035	0.315	0.000	0.098	0.448
		39 GP-3-4	3.701	0.299	1.509	0.362	0.130	2.000	0.017	0.034	0.000	0.180	0.232
		40 GP-3-5	3.834	0.166	1.344	0.278	0.379	2.000	0.000	0.156	0.000	0.194	0.350
		41 GP-3-6	3.690	0.310	1.386	0.367	0.246	2.000	0.000	0.455	0.000	0.051	0.506
		42 GP-3-7	3.751	0.249	1.077	0.576	0.347	2.000	0.000	0.244	0.000	0.176	0.420
		43 GP-3-8	3.919	0.081	1.201	0.369	0.404	1.974	0.000	0.562	0.000	0.000	0.562
		44 GP-3-9	3.919	0.081	1.121	0.435	0.443	2.000	0.000	0.366	0.000	0.079	0.445
		45 GP-3-10	3.847	0.153	1.204	0.383	0.413	2.000	0.000	0.278	0.000	0.144	0.422
		46 GP-3-11	3.861	0.139	1.339	0.296	0.365	2.000	0.035	0.330	0.000	0.052	0.417
47 GP-12-1	3.931	0.069	0.845	0.776	0.379	2.000	0.017	0.103	0.000	0.155	0.276		
48 GP-12-2	3.670	0.330	0.945	0.681	0.373	2.000	0.000	0.262	0.000	0.221	0.483		
49 GP-12-3	3.699	0.301	1.154	0.508	0.338	2.000	0.035	0.438	0.000	0.065	0.539		
50 GP-12-4	3.652	0.348	1.470	0.346	0.184	2.000	0.017	0.104	0.000	0.197	0.318		
51 GP-12-5	4.016	0.000	1.339	0.343	0.318	2.000	0.000	0.103	0.000	0.076	0.179		
52 GP-12-6	4.005	0.000	1.238	0.447	0.316	2.000	0.017	0.069	0.000	0.097	0.183		
53 GP-12-7	4.009	0.000	1.106	0.449	0.445	2.000	0.000	0.121	0.000	0.143	0.264		
54 GP-12-8	4.003	0.000	0.853	0.453	0.661	1.967	0.331	0.087	0.000	0.000	0.418		
55 GP-12-9	3.981	0.019	1.371	0.395	0.234	2.000	0.000	0.069	0.000	0.092	0.161		
56 GP-12-10	3.748	0.252	1.205	0.468	0.326	2.000	0.000	0.121	0.000	0.229	0.350		
57 GP12-2	3.924	0.076	0.792	0.799	0.409	2.000	0.000	0.226	0.000	0.129	0.355		
58 GP12-3	3.488	0.512	1.578	0.397	0.025	2.000	0.000	0.035	0.000	0.251	0.286		
59 GP12-4	3.806	0.194	0.935	0.712	0.352	2.000	0.000	0.139	0.000	0.204	0.343		
60 GP12-5	3.879	0.121	1.259	0.552	0.190	2.000	0.000	0.172	0.000	0.069	0.241		
61 GP12-6	3.941	0.059	1.055	0.720	0.226	2.000	0.000	0.051	0.000	0.117	0.168		
62 GP12-7	3.809	0.191	0.939	0.748	0.313	2.000	0.017	0.191	0.000	0.139	0.348		
63 GP12-8	3.826	0.174	0.835	0.730	0.435	2.000	0.000	0.122	0.000	0.243	0.365		
64 GP12-9	3.618	0.382	1.574	0.329	0.098	2.000	0.035	0.087	0.000	0.162	0.283		
65 GP12-10	4.031	0.000	1.223	0.431	0.346	2.000	0.000	0.155	0.000	0.033	0.188		

837

838

839

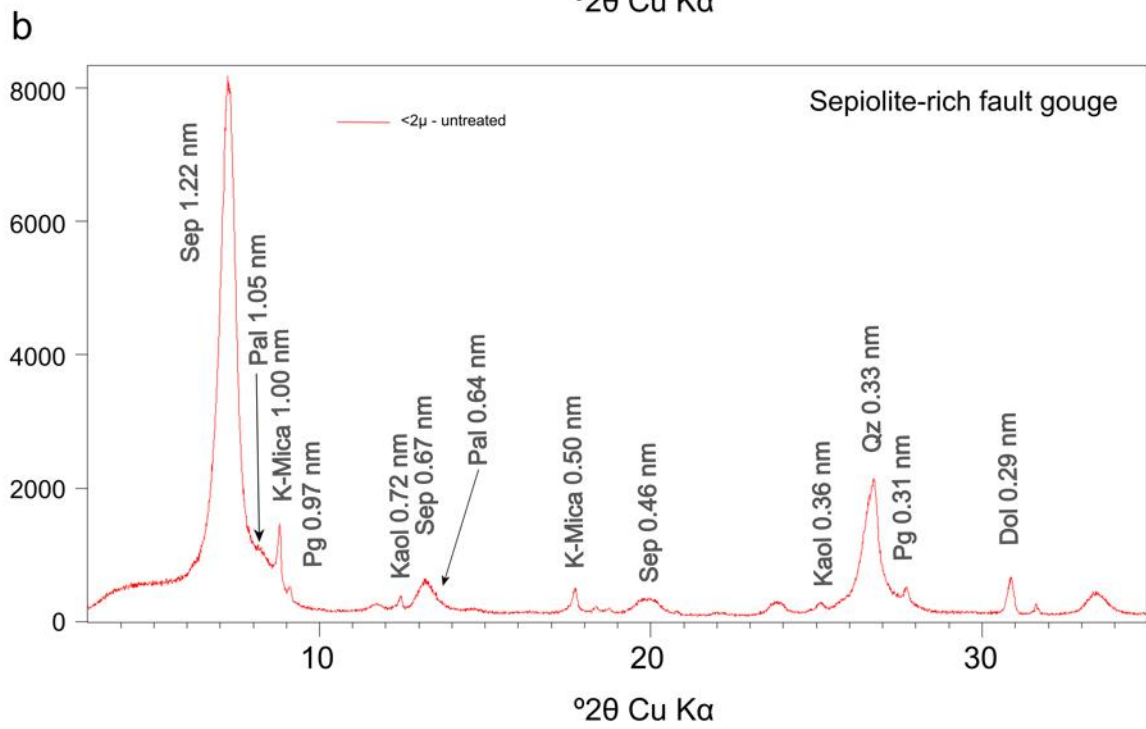
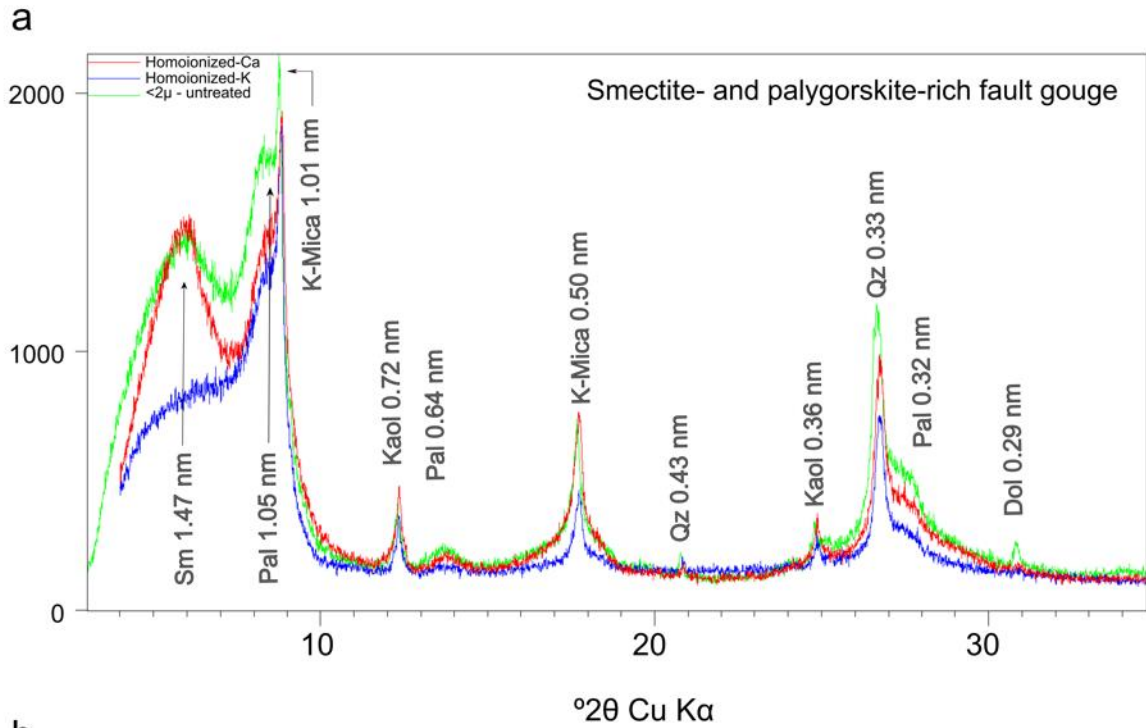
Marls	66 GP1-2	3.873	0.127	1.234	0.436	0.330	2.000	0.035	0.349	0.000	0.019	0.403	
	67 GP1-3	3.644	0.356	1.587	0.226	0.188	2.000	0.035	0.156	0.000	0.159	0.350	
	68 GP1-4	3.725	0.275	1.604	0.191	0.204	2.000	0.052	0.296	0.000	0.040	0.388	
	69 GP1-5	3.550	0.450	1.614	0.192	0.194	2.000	0.052	0.332	0.000	0.103	0.488	
	70 GP1-6	3.767	0.233	1.306	0.467	0.228	2.000	0.000	0.156	0.000	0.152	0.308	
	71 GP1-7	3.775	0.225	1.092	0.527	0.334	1.952	0.105	0.492	0.000	0.000	0.597	
	72 GP1-8	3.759	0.241	1.500	0.278	0.222	2.000	0.000	0.313	0.000	0.074	0.388	
	73 GP1-9	3.946	0.054	1.331	0.363	0.305	2.000	0.000	0.208	0.000	0.076	0.283	
	74 GP1-10	3.756	0.244	1.452	0.329	0.219	2.000	0.035	0.208	0.000	0.093	0.335	
	75 GP1-12	3.855	0.145	1.244	0.434	0.322	2.000	0.069	0.278	0.000	0.025	0.373	
	76 GP1-13	3.623	0.377	1.058	0.613	0.329	2.000	0.123	0.455	0.000	0.003	0.581	
	77 GP1-14	3.980	0.020	1.272	0.431	0.298	2.000	0.069	0.086	0.000	0.047	0.202	
	78 GP1-15	3.582	0.418	1.004	0.650	0.346	2.000	0.140	0.334	0.000	0.075	0.549	
	79 GP1-16	3.990	0.010	1.216	0.403	0.368	1.986	0.088	0.245	0.140	0.000	0.473	
	80 GP1-17	3.849	0.151	1.218	0.416	0.366	2.000	0.052	0.243	0.000	0.085	0.380	
	81 GP1-18	3.834	0.166	1.319	0.363	0.319	2.000	0.138	0.155	0.000	0.027	0.320	
	82 GP1-19	3.716	0.284	1.296	0.417	0.287	2.000	0.104	0.313	0.000	0.025	0.442	
	83 GP1-20	3.672	0.328	1.309	0.383	0.309	2.000	0.104	0.174	0.000	0.127	0.405	
	84 GP1-21	3.843	0.157	1.349	0.329	0.323	2.000	0.069	0.121	0.000	0.110	0.301	
85 GP1-22	3.774	0.226	1.235	0.452	0.313	2.000	0.104	0.296	0.000	0.017	0.417		
86 GP1-23	3.762	0.238	1.305	0.399	0.296	2.000	0.069	0.191	0.000	0.102	0.362		
87 GP1-24	3.687	0.313	1.102	0.629	0.175	1.906	0.210	0.349	0.000	0.000	0.559		
88 GP1-25	3.640	0.360	1.251	0.420	0.280	1.951	0.228	0.333	0.000	0.000	0.560		
Homolized	89 GP3-11	3.722	0.278	0.864	0.544	0.597	2.005	0.316	0.228	0.000	0.000	0.544	
	90 GP3-19	3.522	0.478	1.239	0.336	0.460	2.035	0.177	0.478	0.000	0.000	0.655	
	K	91 GP-3-2	3.579	0.421	1.298	0.368	0.333	2.000	0.158	0.439	0.000	0.000	0.596
		92 GP-3-3	3.664	0.336	1.080	0.389	0.531	2.000	0.159	0.549	0.000	0.000	0.708
		93 GP-3-4	3.890	0.110	1.157	0.451	0.417	2.025	0.087	0.278	0.000	0.000	0.365
		94 GP-3-6	3.863	0.137	1.145	0.537	0.346	2.028	0.104	0.191	0.000	0.000	0.294
		95 GP-3-7	3.397	0.603	1.584	0.196	0.213	1.994	0.053	0.729	0.000	0.000	0.783
		96 GP-3-10	3.632	0.368	1.325	0.419	0.297	2.041	0.140	0.262	0.000	0.000	0.402
		97 GP-3-11	3.843	0.157	1.113	0.522	0.348	1.983	0.174	0.209	0.000	0.000	0.383
		98 GP-3-15	3.806	0.194	1.196	0.539	0.243	1.978	0.087	0.330	0.000	0.000	0.417
		99 GP-3-16	3.745	0.255	1.548	0.210	0.315	2.073	0.000	0.350	0.000	0.000	0.350
		100 GP-3-20	3.783	0.217	1.265	0.366	0.349	1.979	0.157	0.314	0.000	0.000	0.471
		101 GP-3-21	3.849	0.151	1.184	0.624	0.225	2.033	0.035	0.208	0.000	0.000	0.243
102 GP-3-22	3.711	0.289	1.469	0.211	0.299	1.979	0.106	0.440	0.000	0.000	0.545		
103 GP-3-25	3.696	0.304	1.360	0.368	0.228	1.955	0.123	0.420	0.000	0.000	0.543		

840

841

842

843 **Supplementary Figure 1:** Diffractograms of air-dried oriented aggregates of the <2  $\mu\text{m}$  fraction,  
844 for: a. The smectite- and palygorskite-rich fault gouge from Galera Village. and b. The sepiolite-  
845 rich gouge from the Rambla de los Pilares sector. Mineral abbreviations for clay minerals according  
846 to Bergaya et al. (2006), Kaol: kaolinite, K-Mica: white mica (including illite and muscovite), Sep:  
847 sepiolite, Sm: smectite, Pal: palygorskite. Non-clay minerals according to Whitney and Evans  
848 (2010), Chl: chlorite, Dol: dolomite, Pg: paragonite, Qz: quartz. The diffractograms were obtained  
849 in a PANalytical X'Pert Pro diffractometer (CuK $\alpha$  radiation, 45 kV, 40 mA) equipped with an  
850 X'Celerator solid-state linear detector, using a step increment of 0.008 $^\circ$  2 $\theta$  and a counting time of  
851 10 s/step (Department of Mineralogy and Petrology, University of Granada).



852

853